Dalton
Transactions

PAPER

View Article Online
View Journal

Cite this: DOI: 10.1039/c9dt04693c

Structural evolution of the Ru-bms complex to the real water oxidation catalyst of Ru-bda: the bite angle matters†

Jing Yang, Bin Liu and Lele Duan *

Received 10th December 2019,
Accepted 26th February 2020

DOI: 10.1039/c9dt04693c

rsc.li/dalton

Ru-Based complexes have advanced the study of molecular water oxidation catalysts (WOCs) both in catalysis and mechanism. The electronic effect has always been considered as an essential factor for the catalyst properties while less attention has been focused on the bite angle effect on water oxidation catalysis. The **Ru-bda** ([Ru(bda)(pic)$_2$]; bda^{2-} = 2,2′-bipyridine-6,6′-dicarboxylate; pic = 4-picoline) catalyst is one of the most active WOCs and it has a largely distorted octahedral configuration with an O–Ru–O bite angle of 123°. Herein, we replaced the carboxylate (–COO$^-$) groups of bda^{2-} with two methylenesulfonate (–$CH_2SO_3^-$) groups and prepared a negatively charged ligand, bms^{2-} (2,2′-bipyridine-6,6′-dimethanesulfonate), and the **Ru-bms** complex [Ru(bms)(pic)$_2$]. The O–Ru–O bite angle changed from 123° in **Ru-bda** to 84° in **Ru-bms**, leading to a dramatic influence on the catalytic behavior. Systematic analysis of the reaction intermediates suggested that **Ru-bms** transformed all the way to **Ru-bda** *via* oxidative decomposition under Ce^{IV}-driven water oxidation conditions.

Introduction

Currently, the main global energy supply is provided by fossil fuels, and the heavy dependence on these finite resources has caused a severe energy crisis and environmental pollution.[1,2] Considering that water can be split into O_2 and H_2 by solar energy, this so-called water-splitting process is actually one of the most promising ways to meet the energy demands of humanity. Furthermore, two half-reactions are usually involved in the water-splitting process: water oxidation ($2H_2O \rightarrow O_2 + 4H^+ + 4e^-$) and proton reduction ($4H^+ + 4e^- \rightarrow 2H_2$); the former reaction is considered as the bottleneck of the process due to the transfer of four electrons and O–O bond formation.[3] Importantly, two different pathways of O–O bond formation, water nucleophilic attack (WNA) and interaction of two metal oxo species (I2M), have been proposed.[4]

Homogenous systems possess superiority over heterogeneous systems of bridging a rational designed molecular structure with a well-defined reaction mechanism, which, in turn, affords catalyst optimization and innovation. In recent years, water oxidation catalysts (WOCs) based on transition metal complexes involving Ru,[5,6] Mn,[7,8] Fe,[9–11] Cu,[12–14] Co[15] and Ni[16] have attracted considerable attention. Among these, both dinuclear and mononuclear Ru-based WOCs with polypyridyl ligands,[3,17] such as the blue dimer,[5] the **Ru-Hbpp** catalyst (Hbpp$^-$ = 3,5-bis(2-pyridyl)pyrazolato ligand)[18] and **Ru-bnp** (bnp = 4-*tert*-butyl-2,6-di([1′,8′]-naphthyrid-2′-yl)pyridine),[6] have achieved the greatest success, and even a metallosupramolecular macrocycle that gathers three Ru(bda) centers has exhibited remarkable catalysis.[19] By utilizing a strongly electron-donating dianionic ligand, 2,2′-bipyridine-6,6′-dicarboxylate (bda^{2-}), Sun and co-workers reported a series of highly active **Ru-bda** WOCs, with turnover frequency (TOF) numbers up to 1000 s^{-1} under acidic conditions with cerium(IV) ammonium nitrate (Ce^{IV}) as a sacrificial chemical oxidant.[20–23] Later on, phosphate groups were introduced by Concepcion and co-workers to give **Ru-bpaH$_2$** (bpaH$_2$$^{2-}$ = 2,2′-bipyridine-6,6′-diphosphonate, O–Ru^{III}–O: 112°) and **Ru-bpHc** (bpHc^{2-} = 6′-phosphono-[2,2′-bipyridine]-6-carboxylate, O–Ru^{III}–O: 117°) with the latter having a TOF of 100 s^{-1} (Fig. 1).[24,25] The Llobet group developed the **Ru-tda** (tda^{2-} = [2,2′:6′,2″-terpyridine]-6,6″-dicarboxylate, O–Ru^{III}–N: 142°) complex with one dangling carboxylate group as an internal base, and this catalyst displayed high electrochemical water oxidation efficiency under neutral conditions, during which the tda^{2-} ligand facilitates the formation of seven-coordinate Ru species.[26]

Minor modification of the ligand environments of **Ru-bda** gives rise to significant differences toward catalytic water oxidation.[27] The replacement of axial ligands of **Ru-bda** from

---

Department of Chemistry, Shenzhen Grubbs Institute and Guangdong Provincial Key Laboratory of Energy Materials for Electric Power, Southern University of Science and Technology (SUSTech), Shenzhen, 518055, P. R. China.
E-mail: duanll@sustech.edu.cn

† Electronic supplementary information (ESI) available: X-ray crystallographic data in table. CCDC 1968200. For ESI and crystallographic data in CIF or other electronic format see DOI: 10.1039/c9dt04693c

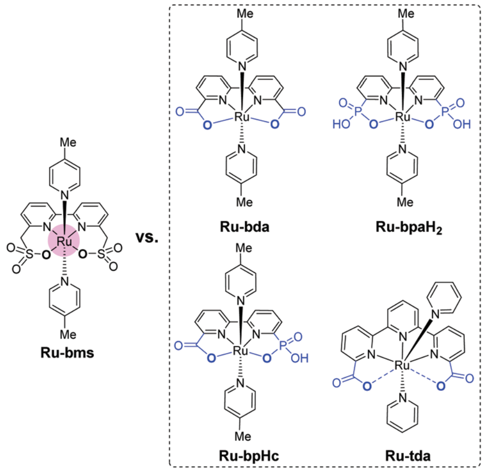

Fig. 1 Molecular structures of **Ru-bms** synthesized in the current work (left) and the previously synthesized complexes **Ru-bda**, **Ru-bpaH$_2$**, **Ru-bpHc**, and **Ru-tda** (right).

4-picoline to isoquinoline resulted in a dramatic promotion of the TOF from 32 s^{-1} to 303 s^{-1}.[21] By changing the equatorial ligand of **Ru-bda** from a flexible bda^{2-} ligand to a rigid pda^{2-} (H_2pda = 1,10-phenanthroline-2,9-dicarboxylic acid) ligand, Ce^{IV}-driven water oxidation changes from the binuclear to the mononuclear pathway.[28] Notably, the large bite angle of O–Ru–O is essential for direct coordination of a water molecule at the seventh position to the highly valent Ru center, which is a crucial step for the **Ru-bda** catalysts to access higher oxidation states of the metal center through the proton-coupled electron transfer (PCET) process.[29,30] Especially, the seven-coordinate intermediate Ru^{IV}–OH has been confirmed by X-ray crystallography for **Ru-bda** with a bite angle of 123°.[20] Therefore, we were motivated to investigate whether changing the large O–Ru–O cleft of **Ru-bda** from 123° to nearly 90° of an ideal octahedral configuration would give any insight into the structure–mechanism–activity relationship.

Given the above considerations, we designed herein a negatively charged ligand, 2,2′-bipyridine-6,6′-dimethanesulfonate (bms^{2-}), and reported its Ru complex $[Ru(bms)(pic)_2]$ (**Ru-bms**; Fig. 1) toward water oxidation. The **Ru-bms** complex displayed a smaller O–Ru–O bite angle than the **Ru-bda** complex. The O–Ru–O bite angle has a dramatic effect on the water oxidation activity. Under Ce^{IV}-driven water oxidation conditions, the **Ru-bms** complex is a precatalyst and undergoes multiple oxidative decomposition steps to form the real water oxidation catalyst, the **Ru-bda** catalyst. The O–Ru–O bite angle indeed plays a vital role in the transition metal complex-catalyzed water oxidation reaction.

Experimental

Chemicals and starting materials

All solvents and chemicals are commercially available and were used without further purification. The water used in all reactions was purified by a water purification system. *cis*-$[Ru(DMSO)_4Cl_2]$ was prepared according to the literature method.[31] The ligand disodium 2,2′-bipyridine-6,6′-dimethanesulfonate (Na_2bms) was synthesized on the basis of the literature procedures.[32]

Ru-bms: Na_2bms (271.8 mg, 0.7 mmol) and *cis*-$[Ru(DMSO)_4Cl_2]$ (338.8 mg, 0.7 mmol) were placed in a mixed solvent of methanol (24 mL) and water (12 mL), then degassed with N_2 and refluxed over 8 h. The solvent was removed and replaced by methanol (20 mL). An excess of 4-picoline (0.7 mL) was added and the reflux was continued for an additional 4 h. Solvent was then removed, and the resulting mixture was purified by column chromatography on silica gel using mixed methanol and dichloromethane as eluents (1/20 in volume), yielding **Ru-bms** as a dark red solid (221 mg, yield = 50%). ^1H NMR (400 MHz, d_4-methanol, Fig. S1†): δ 8.63 (d, J = 7.7 Hz, 2H), 7.99–7.78 (m, 6H), 7.40 (d, J = 7.4 Hz, 2H), 7.05 (d, J = 6.2 Hz, 4H), 4.02 (s, 4H), 2.32 (s, 6H). High-resolution mass (Fig. S2†): m/z^+ = 631.0242 $(M + H^+)$, calcd: 631.0254 Elemental analysis: Calcd for $C_{24}H_{24}N_4O_6RuS_2{\cdot}2H_2O$: C 43.30%, H 4.24%, N 8.42%; found: C 43.44%, H 4.06%, N 8.21%.

Physical methods

^1H NMR spectra were recorded on a 400 MHz Bruker Advance spectrometer. Elemental analyses were acquired with a Thermo-quest-Flash EA 1112 apparatus. Electrochemical measurements were performed with a CHI760 electrochemical workstation, using a glassy carbon disk (φ = 3 mm) as the working electrode, a platinum column as the counter electrode, and an aqueous saturated Ag/AgCl electrode as the reference electrode. All potentials reported herein were referenced to NHE (E(Ag/AgCl) = 210 mV *vs.* NHE). All the buffer solutions used in the electrochemistry study are phosphate buffers. The generated oxygen was detected by a pressure transducer (MIK-P300) driven at 10.00 V using a power supply (HY3005B) plus a data acquisition module (Omega OM-DAQ-USB-2401). A solution of Ce^{IV} in 0.1 M CF_3SO_3H (3.0 mL) was added into the flask, then an aqueous solution of the catalyst (1 mM) was injected into the above solution under vigorous stirring at ambient temperature (25 ± 1 °C).

Mass spectrometry measurements to capture the Ru intermediates were performed using a Thermo Scientific LCQ Fleet mass spectrometer. In an acid solution of **Ru-bms** (0.67 mM), 10 equivalents of Ce^{IV} was added, and the reaction solution was then directly injected into the mass spectrometer by a continuous injection syringe. High-resolution mass spectrometry measurements were performed on a Thermo Scientific Q Exactive mass spectrometer. The single-crystal X-ray diffraction data were collected on a Bruker Smart Apex II CCD diffractometer with graphite-monochromated Mo-K_α radiation (λ = 0.71073 Å) at 296 K. The structure was solved by direct methods using SHELXS and refined by full-matrix least-squares on the $|F^2|$ algorithm (SHELXL) using the Olex2 program.

Results and discussion

Synthesis and characterization

We initially attempted to prepare ([2,2′-bipyridine]-6,6′-diyl)diacetic acid (**L1**) and its Ru complex. However, due to the synthetic challenge of this ligand, we changed our plan and prepared Na_2bms instead of the diacetic ligand. The ligand Na_2bms was prepared according to the literature method and its synthetic procedures are shown in Scheme 1. Deprotonation of 6,6′-dimethyl-2,2′-bipyridine followed by chlorination affords 6,6′-bis(chloromethyl)-2,2′-bipyridine, and then this intermediate is treated with sodium sulphite to yield the desired ligand as a disodium salt.[32] The synthesis of **Ru-bms** was achieved by the reaction of Na_2bms and *cis*-$[Ru(DMSO)_4Cl_2]$ (DMSO = dimethyl sulfoxide) in the presence of methanol and H_2O, followed by addition of excess 4-picoline (Scheme 1). The complex was thoroughly characterized by X-ray crystallography, ^{1}H NMR spectroscopy, elemental analysis, mass spectrometry and electrochemistry.

The X-ray crystallography of **Ru-bms** is depicted in Fig. 2. There are two ruthenium molecules and five solvate water molecules in the asymmetric unit of the crystal lattice. The metal center of Ru^{II} adopts an octahedral geometry and the bms^{2-} ligand is in a tetradentate manner occupying the equatorial position of the Ru center while two 4-picoline moieties are situated at the axial positions. The Ru–O bond lengths of **Ru-bms** span from 2.137 to 2.161 Å, slightly smaller than those of **Ru-bda** (2.172 and 2.216 Å). Notably, the O11–Ru1–O12 bite angle of **Ru-bms** is 84°, close to the ideal 90° of an octahedral configuration. This angle is much smaller than that of the previously reported **Ru-bda** catalyst with an O–Ru–O angle of 123°. Therefore, it would be difficult for **Ru-bms** to form seven-coordinate Ru intermediates during the water oxidation process, and thus the bite angle indeed has a dramatic influence on the catalytic activity. Additionally, there are more non-coordinated oxygen atoms from sulfonate group hydrogen-bonding to the lattice water molecules with the shortest non-bonded O⋯O separation being about 2.756 Å, typical of O–H⋯O hydrogen-bonding.

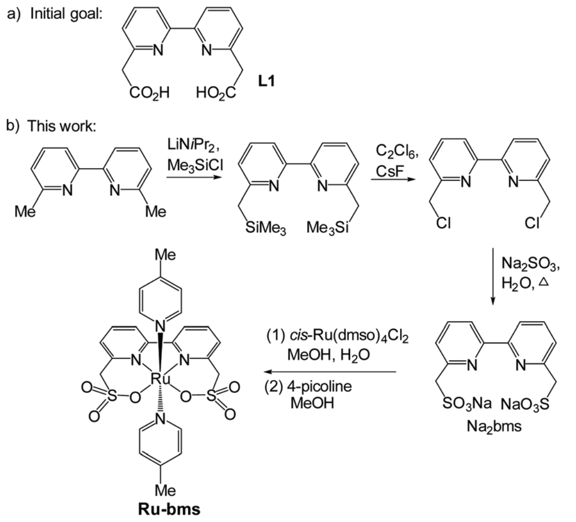

Scheme 1 (a) The initial goal of ligand **L1** and (b) the synthetic routes of Na_2bms and **Ru-bms** in this work.

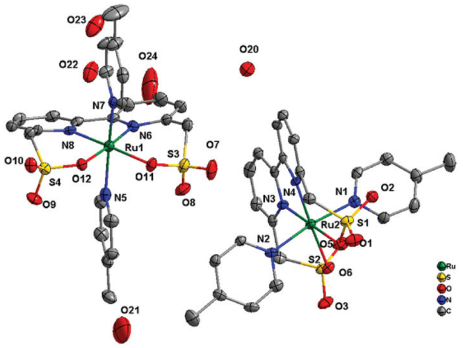

Fig. 2 The X-ray crystal structure of **Ru-bms** with thermal ellipsoids at the 50% probability level (hydrogen atoms are omitted for clarity). The oxygen atoms O20, O21, O22, O23, and O24 are from solvate water molecules.

Ligand exchange

Ru-bms has strong resistance against ligand exchange, which was examined in various deuterated solvents. The ^{1}H NMR spectrum of **Ru-bms** (Fig. 3a) in D_2O/d_4-methanol (1/1, v/v) agrees with the C_{2v} symmetry of its proposed structure. In the aromatic region, three peaks at 8.64 (d, 2H), 7.97 (d, 2H), and 7.44 (d, 2H) ppm represent the proton resonances of bms^{2-}, and two doublets at 7.80 (d, 4H) and 7.09 (d, 4H) ppm are attributed to the aromatic protons of two axial 4-picoline ligands. With the use of D_2O/d_3-acetonitrile or d_3-acetonitrile (Fig. 3b and c), most of these peaks showed observable upfield shifts but without the formation of new peaks. The C_{2v} symmetry remains, suggesting that the coordinated methylenesulfonate group cannot be replaced by acetonitrile in the Ru^{II} state. However, in the case of **Ru-bda** in mixed D_2O/d_3-acetonitrile, one carboxylate of the bda^{2-} ligand could dissociate from the Ru center to result in the product of a zwitterionic, acetonitrile-coordinating complex, $[Ru(\kappa_3^{O,N,N}\text{-bda})(pic)_2(NCCH_3)]$.[33,34] Taking into consideration that **Ru-bda** adopts a strongly distorted octahedral configuration with a

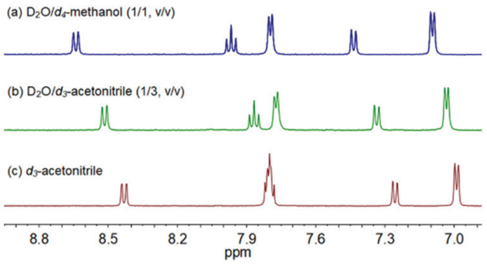

Fig. 3 Aromatic region of ^{1}H NMR spectra of **Ru-bms** in different deuterated media: (a) D_2O/d_4-methanol (1/1, v/v), (b) D_2O/d_3-acetonitrile (1/3, v/v) and (c) d_3-acetonitrile.

very large O–Ru–O angle, this could trigger considerable steric tension between the bda^{2-} ligand and Ru^{II}. Accordingly, this appears to lengthen the distance of Ru–O bonds for **Ru-bda** so as to weaken the coordination bond between O and Ru^{II}. In contrast, the strong binding of the equatorial bms^{2-} ligand to the Ru center is probably due to the fact that **Ru-bms** shows a pseudo-octahedral structure that greatly facilitates decreasing the tension and makes the complex more stable against ligand substitution.

Electrochemistry

Cyclic voltammetry (CV) and differential pulse voltammetry (DPV) were used to electrochemically characterize **Ru-bms** in pH 1.0 and pH 7.0 aqueous solutions. Under acidic conditions, as exhibited in Fig. 4a, one reversible peak appeared at 0.96 V (*vs.* normal hydrogen electrode, NHE), corresponding to the redox process of Ru$^{III/II}$. The DPV of **Ru-bms** in the range of 1.6 to 1.8 V revealed two extra oxidation peaks that are not clearly separated from each other and could be tentatively assigned to the oxidation process to higher valent Ru states. We propose that the Ru═O species (most likely Ru^{V}═O) is generated at such high applied potentials because we observed the C–H bond oxidation of **Ru-bms** when Ce^{IV} (E(Ce$^{IV/III}$) = 1.61 V *vs.* NHE)[35] was used as a chemical oxidant (see below). A large current enhancement is observed above 1.6 V, indicating the presence of catalytic oxidation of water and/or ligand. Thereby, although **Ru-bms** is stable against acetonitrile coordination in the Ru^{II} state, its high valence oxo species could still be generated, indicating that water is accessible to the metal center at high oxidation states. In pH 7.0 phosphate buffer solutions (Fig. 4b), the oxidation potential of Ru$^{III/II}$ remains at 0.98 V while the second and third oxidation waves (see the DPV curve) shifted to a lower oxidation potential. A dramatic enhancement in the catalytic current is achieved above 1.3 V. In comparison, **Ru-bda** displays clearly separated Ru$^{III/II}$ and Ru$^{IV/III}$ waves prior to the water-oxidation onset,[21,36] which is likely due to the relatively weaker electron-donating ability of the methylenesulfonate group than the carboxylate group.

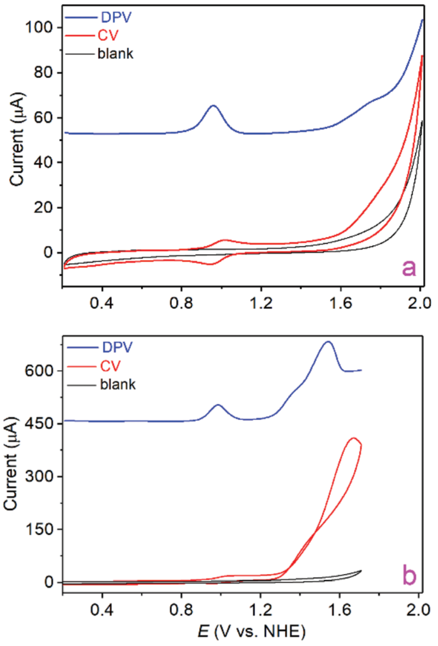

Fig. 4 CVs (red curve) and DPVs (blue curve) of **Ru-bms** (1 mM) in (a) pH 1.0 triflic acid aqueous solution with a scanning rate of 20 mV s^{-1} and (b) pH 7.0 0.2 M phosphate buffer solution (I = 0.5 M (NaNO$_3$)) with a scanning rate of 100 mV s^{-1}. The diameter of the glassy carbon working electrode is 3 mm. The blank data are shown by a black line.

Meyer and co-workers have reported that the added base HPO$_4^{2-}$ plays an important role in electrochemical water oxidation by Ru-based WOCs.[34] Accordingly, an investigation was carried out by maintaining **Ru-bms** at 0.2 mM, a pH value of 7.0 and an ionic strength of 0.5 M with addition of NaNO$_3$ while increasing the concentration of buffer (H$_2$PO$_4^-$ + HPO$_4^{2-}$) from 0.01 M to 0.20 M. Significant acceleration of catalytic current toward water oxidation upon addition of proton acceptor bases was observed, as shown in Fig. 5. As indicated in Fig. 6, the CV measurements in pH 7.0 buffer reveal a linear dependence of the ratio (i_{cat}/i_p)^2 on HPO$_4^{2-}$ in which i_p is the peak current for the Ru^{II} → Ru^{III} wave that is measured at E_p = 1.03 V and i_{cat} is measured at $E_{p,a}$ = 1.35 V. This is in concert with the equation $\left(\frac{i_{cat}}{i_p}\right)^2 = \frac{2.07}{\nu}(k_{H_2O} + k_B[B])$ with $k_{HPO_4^{2-}} = 2.86 \pm 0.16\ M^{-1}\ s^{-1}$, as illustrated by the slope, and $k_{H_2O} = 0.04\ s^{-1}$, as elucidated from the intercept, where k_{H_2O} is the rate constant for unassisted water oxidation and k_B is the contribution from the proton acceptors, H$_2$PO$_4^-$ and HPO$_4^{2-}$. Kinetic enhancements provided by the added proton bases originate from the involvement of the PCET effect with electron transfer to the electrode occurring along with proton transfer to the added base in the rate-limiting step.

Ce^{IV}-Driven water oxidation

The Ce^{IV}-driven water oxidation by **Ru-bms** was further investigated using Ce^{IV} as an oxidant in acid aqueous solutions.

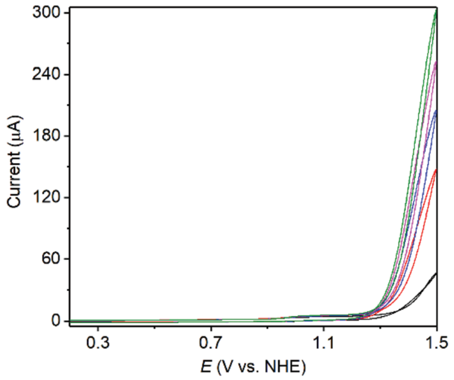

Fig. 5 CVs of 0.2 mM **Ru-bms** at pH 7.0 in H$_2$PO$_4^-$/HPO$_4^{2-}$ buffers, and buffer concentrations are 0.01 M (black), 0.05 M (red), 0.10 M (blue), 0.15 M (magenta), and 0.20 M (green), I = 0.5 M (NaNO$_3$), scan rate is 20 mV s^{-1}.

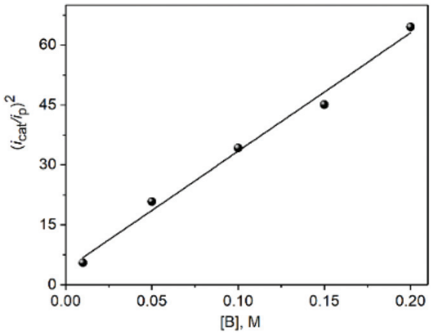

Fig. 6 Plots of k_{obs} *vs.* buffer base concentration in $H_2PO_4^-/HPO_4^{2-}$ buffer at pH 7.0. [**Ru-bms**] = 0.2 mM, I = 0.5 M ($NaNO_3$), scan rate is 20 mV s^{-1}.

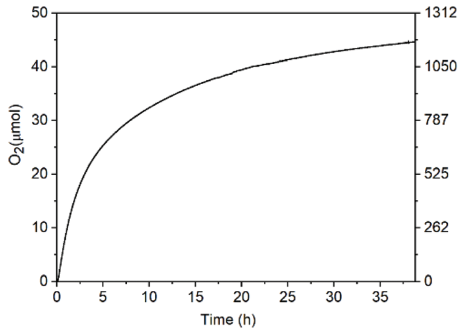

Fig. 7 Oxygen evolution curve. [Ce^{IV}] = 0.083 M, [Cat.] = 12.7 μM, and V = 3 mL, pH 1.0 triflic acid aqueous solution.

Fig. 7 depicts the plots of oxygen evolution *versus* time, and the corresponding TON of **Ru-bms** was calculated to be 1171 after running for 39 hours. Specifically, **Ru-bms** displayed a much longer lifetime than **Ru-bda** (less than an hour). However, due to its small TOF number (0.05 s^{-1}; see below), **Ru-bms** gives a moderate TON. Nevertheless, the performance of **Ru-bms** is comparable with other Ru-based WOCs other than **Ru-bda** under Ce^{IV}-driven water oxidation conditions.

To get kinetic information on oxygen evolution, concentration-dependent catalytic investigations were carried out. It is worth noting here that there was an initial lag phase before O_2 evolution under water oxidation conditions (Fig. 8a), indicating that **Ru-bms** is not the real catalyst and it has to evolve to other real WOCs. After the induction period, O_2 evolved linearly with time, and measurements of kinetic study revealed that the rate of oxygen evolution under catalytic conditions shows a nearly linear dependence on the catalyst concentration, providing evidence for an apparent pseudo first-order kinetic rate = k_{O_2}[Cat.] ([Ce^{IV}] is in large excess; Fig. 8b). The TOF of **Ru-bms** could be defined as the first-order rate constant of O_2 evolution, k_{O_2}, which was determined as 0.05 s^{-1}.

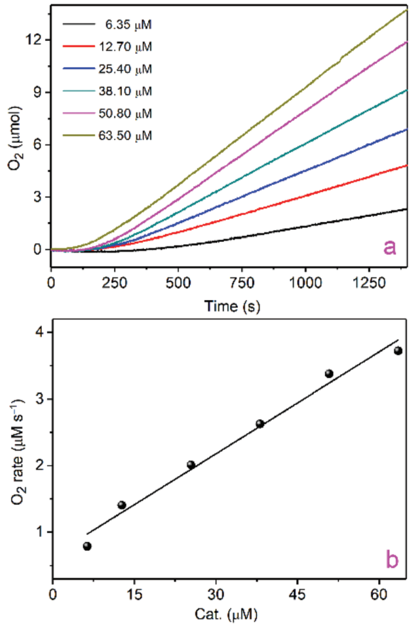

Fig. 8 (a) Oxygen evolution curve at various concentrations of catalyst. [Ce^{IV}] = 0.083 M, [Cat.] = 12.7–63.5 μM. (b) O_2 rate *versus* [Cat.] based on the plots of oxygen evolution in the interval of 550–1050 s. All experiments were carried out in pH 1.0 triflic acid aqueous solution at 298 K with a total volume of 3 mL.

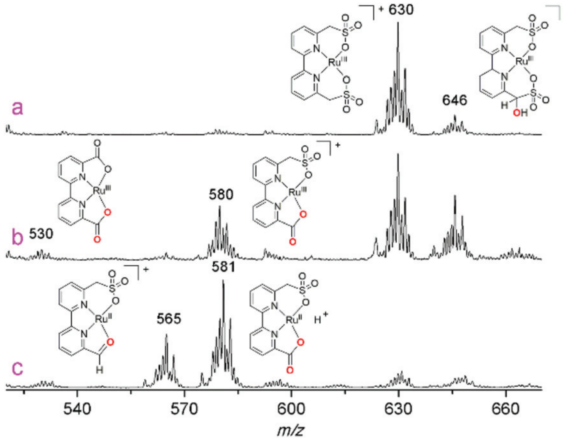

Fig. 9 (a) MS spectra of **Ru-bms** (0.67 mM) with additional 10 equivalents of Ce^{IV} in pH 1.0 triflic acid aqueous solutions were recorded (a) immediately, (b) after 35 min, and (c) after subsequent treatment with 2 equivalents of ascorbic acid after 70 min (the axial ligands of complexes are omitted for clarity).

Capture reaction intermediates

ESI-mass spectrometry was used to capture the reaction intermediates during Ce^{IV}-driven water oxidation by **Ru-bms** (Fig. 9). The mass spectra were obtained at different time intervals after addition of 10 equivalents of Ce^{IV} in pH 1.0 triflic acid aqueous solutions. Two major products were observed at m/z = 630 and 646, which well fit the structures of $[Ru^{III}(SO_3\text{-}CH_2\text{-bpy-}CH_2\text{-}SO_3)(pic)_2]^+$ and $[Ru^{III}(SO_3\text{-}CH_2\text{-bpy-CHOH-}SO_3)(pic)_2]^+$, respectively (Fig. 9a, 10a and b). Peaks with one additional O atom are usually assigned as oxo species, such as $[Ru^V(O)(SO_3\text{-}CH_2\text{-bpy-}CH_2\text{-}SO_3)(pic)_2]^+$, but this is inapplicable in this case (see below). When the solution was kept for

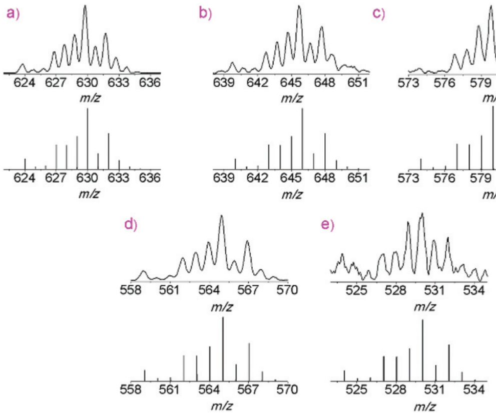

Fig. 10 The experimental (top) and calculated (bottom) isotopic patterns of (a) $[Ru^{III}(SO_3\text{-}CH_2\text{-bpy-}CH_2\text{-}SO_3)(pic)_2]^+$, (b) $[Ru^{III}(SO_3\text{-}CH_2\text{-bpy-CHOH-}SO_3)(pic)_2]^+$, (c) $[Ru^{III}(SO_3\text{-}CH_2\text{-bpy-}CO_2)(pic)_2]^+$, (d) $[Ru^{II}(SO_3\text{-}CH_2\text{-bpy-CHO})(pic)_2]^+$ and (e) $[Ru^{III}(bda)(pic)_2]^+$.

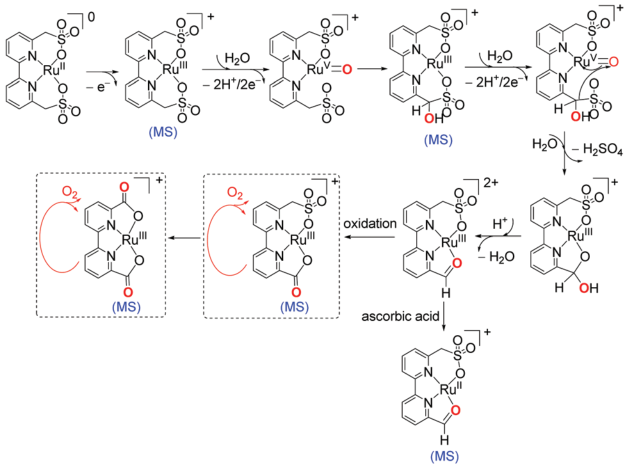

Fig. 11 Proposed oxygen generation pathways under the catalytic conditions with Ce^{IV} as oxidant at pH 1.0. The dashed lines indicate the two active species toward water oxidation.

35 min, its MS spectrum started to show changes. Most of the original peaks reduced in intensity spontaneously while a new peak at m/z = 580 appeared gradually and increased in intensity where the Ru^{III} species was assigned as the six-coordinate $[Ru^{III}(SO_3\text{-}CH_2\text{-bpy-}CO_2)(pic)_2]^+$ with one carboxylate arm coordinated instead of the original methylenesulfonate group (Fig. 9b and 10c). Another peak at m/z = 530 with very weak intensity was attributed to $[Ru^{III}(bda)(pic)_2]^+$ (Fig. 9b and 10e). Upon subsequent addition of 2 equivalents of ascorbic acid after 70 min (Fig. 9c), the above solution exists predominantly as a mixture of $[Ru^{II}(SO_3\text{-}CH_2\text{-bpy-}CO_2)(pic)_2 + H]^+$ (m/z = 581) and new species $[Ru^{II}(SO_3\text{-}CH_2\text{-bpy-CHO})(pic)_2]^+$ (m/z = 565, Fig. 10d) together with a little $[Ru^{III}(bda)(pic)_2]^+$, whereas the original species of $[Ru^{III}(SO_3\text{-}CH_2\text{-bpy-}CH_2\text{-}SO_3)(pic)_2]^+$ and $[Ru^{III}(SO_3\text{-}CH_2\text{-bpy-CHOH-}SO_3)(pic)_2]^+$ almost disappeared. If the aforementioned signal at m/z = 646 is the Ru^V oxo species, it should be reduced to $[Ru^{II}(SO_3\text{-}CH_2\text{-bpy-}CH_2\text{-}SO_3)(pic)_2 + H]^+$ by ascorbic acid but this signal remained. Thereby, this species at m/z = 646 is ascribed to the C–H bond oxidized species, $[Ru^{III}(SO_3\text{-}CH_2\text{-bpy-CHOH-}SO_3)(pic)_2]^+$. Additionally, as shown in Fig. 10, all of their experimental and calculated isotopic patterns match well with each other.

Evolution of Ru-bms

On the basis of MS analysis together with the documented Ru═O catalyzed C–H bond activation,[37] the structural evolution of **Ru-bms** under Ce^{IV}-driven water oxidation conditions is proposed in Fig. 11. At pH 1.0, the first oxidation of the initial $[Ru^{II}]^0$ gives $[Ru^{III}]^+$; then, water nucleophilic attack on $[Ru^{III}]^+$ by substituting a coordinated sulfonate ligand along with PCET oxidation steps affords a tentative Ru^V═O species (Ru^{IV}═O is also possible but Ru^V═O is more common when anionic ligands are used in the coordiantion sphere; we were not able to obtain any experimental evidence on the high valent Ru species) with a dangling methylenesulfonate arm. The subsequent oxidation of the C–H bond of the dangling methylenesulfonate occurs to generate $[Ru^{III}(SO_3\text{-}CH_2\text{-bpy-CHOH-}SO_3)(pic)_2]^+$. The oxidation of the Ru center occurs and the Ru^V═O species $[Ru^V(O)(SO_3\text{-}CH_2\text{-bpy-CHOH-}SO_3)(pic)_2]^+$ is formed with a sulfonate arm uncoordinated. Intramolecular oxidation of the C–S bond by the oxo group leads to the formation of $[Ru^{III}(SO_3\text{-}CH_2\text{-bpy-CHOH-O})(pic)_2]^+$ and the released SO_3 further reacts with water to form H_2SO_4. The protonation and dehydration of $[Ru^{III}(SO_3\text{-}CH_2\text{-bpy-CHOH-O})(pic)_2]^+$ give the aldehyde species $[Ru^{III}(SO_3\text{-}CH_2\text{-bpy-CHO})(pic)_2]^{2+}$. Further oxidation of the aldehyde species gives the intermediates of $[Ru^{III}(SO_3\text{-}CH_2\text{-bpy-}CO_2)(pic)_2]^+$ and $[Ru^{III}(bda)(pic)_2]^+$, which could be active species toward water oxidation. Apparently, the formation of **Ru-bda** is slow, which could explain the slow oxygen formation in the Ce^{IV}-driven water oxidation. In addition, $[Ru^{III}(SO_3\text{-}CH_2\text{-bpy-}CO_2)(pic)_2]^+$ might also be active toward water oxidation but with low activity, and it may catalyze the O–O bond formation *via* the WNA pathway. Our hypothesis can explain the first-order kinetics of oxygen evolution with a low TOF value.

Conclusions

In summary, the mononuclear **Ru-bms** incorporating methylenesulfonate groups was prepared to study the bite angle effect on water oxidation. Decreasing the O–Ru–O bite angle reduced the tension in the bipyridine ring of **Ru-bms** and enhanced the stability of **Ru-bms** against acetonitrile coordination. Upon changing the O–Ru–O bite angle from 123° to 84°, **Ru-bms** became inactive toward water oxidation and it transformed to a series of Ru complexes, as evidenced by mass spectrometry experiments. Three intermediates, $[Ru^{III}(SO_3\text{-}CH_2\text{-bpy-CHOH-}SO_3)(pic)_2]^+$, $[Ru^{III}(SO_3\text{-}CH_2\text{-bpy-}CO_2)(pic)_2]^+$ and $[Ru^{III}(bda)(pic)_2]^+$, were detected when **Ru-bms** was oxidized by Ce^{IV} in acidic medium, where the latter two were proposed as the active species for water oxidation. This work sheds light on the bite angle effect on the structure–mechanism–property relationship and provides new guidelines for the design of active water oxidation catalysts – the bite angle matters.

Conflicts of interest

There are no conflicts to declare.

Acknowledgements

This work is supported by the National Natural Science Foundation of China (21771098), the Science and Technology Innovation Commission of Shenzhen Municipality (JCYJ20170817111548026), the Guangdong Provincial Key Laboratory of Energy Materials for Electric Power (2018B030322001) and the Shenzhen Nobel Prize Scientists Laboratory Project (C17783101). The authors would like to gratefully acknowledge Dr Xiaoyong Chang at SUSTech for the X-ray crystal data refinement.

Notes and references

1 P. Garrido-Barros, C. Gimbert-Surinach, R. Matheu, X. Sala and A. Llobet, *Chem. Soc. Rev.*, 2017, **46**, 6088–6098.

2 M. D. Kärkäs, O. Verho, E. V. Johnston and B. Åkermark, *Chem. Rev.*, 2014, **114**, 11863–12001.

3 L. Duan, L. Wang, F. Li, F. Li and L. Sun, *Acc. Chem. Res.*, 2015, **48**, 2084–2096.

4 D. W. Shaffer, Y. Xie and J. J. Concepcion, *Chem. Soc. Rev.*, 2017, **46**, 6170–6193.

5 S. W. Gersten, G. J. Samuels and T. J. Meyer, *J. Am. Chem. Soc.*, 1982, **104**, 4029–4030.

6 R. Zong and R. P. Thummel, *J. Am. Chem. Soc.*, 2005, **127**, 12802–12803.

7 L. Ma, Q. Wang, W. L. Man, H. K. Kwong, C. C. Ko and T. C. Lau, *Angew. Chem., Int. Ed.*, 2015, **54**, 5246–5249.

8 K. J. Young, B. J. Brennan, R. Tagore and G. W. Brudvig, *Acc. Chem. Res.*, 2015, **48**, 567–574.

9 M. K. Coggins, M. T. Zhang, A. K. Vannucci, C. J. Dares and T. J. Meyer, *J. Am. Chem. Soc.*, 2014, **136**, 5531–5534.

10 L. D. Wickramasinghe, R. W. Zhou, R. F. Zong, P. Vo, K. J. Gagnon and R. P. Thummel, *J. Am. Chem. Soc.*, 2015, **137**, 13260–13263.

11 J. L. Fillol, Z. Codola, I. Garcia-Bosch, L. Gomez, J. J. Pla and M. Costas, *Nat. Chem.*, 2011, **3**, 807–813.

12 X. J. Su, M. Gao, L. Jiao, R. Z. Liao, P. E. M. Siegbahn, J. P. Cheng and M. T. Zhang, *Angew. Chem., Int. Ed.*, 2015, **54**, 4909–4914.

13 Y. J. Liu, Y. Z. Han, Z. Y. Zhang, W. Zhang, W. Z. Lai, Y. Wang and R. Cao, *Chem. Sci.*, 2019, **10**, 2613–2622.

14 S. J. Koepke, K. M. Light, P. E. VanNatta, K. M. Wiley and M. T. Kieber-Emmons, *J. Am. Chem. Soc.*, 2017, **139**, 8586–8600.

15 H. Y. Du, S. C. Chen, X. J. Su, L. Jiao and M. T. Zhang, *J. Am. Chem. Soc.*, 2018, **140**, 1557–1565.

16 M. Zhang, M.-T. Zhang, C. Hou, Z.-F. Ke and T.-B. Lu, *Angew. Chem., Int. Ed.*, 2014, **53**, 13042–13048.

17 L. P. Tong and R. P. Thummel, *Chem. Sci.*, 2016, **7**, 6591–6603.

18 C. Sens, I. Romero, M. Rodriguez, A. Llobet, T. Parella and J. Benet-Buchholz, *J. Am. Chem. Soc.*, 2004, **126**, 7798–7799.

19 M. Schulze, V. Kunz, P. D. Frischmann and F. Würthner, *Nat. Chem.*, 2016, **8**, 576–583.

20 L. Duan, A. Fischer, Y. Xu and L. Sun, *J. Am. Chem. Soc.*, 2009, **131**, 10397–10399.

21 L. Duan, F. Bozoglian, S. Mandal, B. Stewart, T. Privalov, A. Llobet and L. Sun, *Nat. Chem.*, 2012, **4**, 418–423.

22 L. Wang, L. Duan, B. Stewart, M. Pu, J. Liu, T. Privalov and L. Sun, *J. Am. Chem. Soc.*, 2012, **134**, 18868–18880.

23 L. Wang, L. Duan, Y. Wang, M. S. G. Ahlquist and L. Sun, *Chem. Commun.*, 2014, **50**, 12947–12950.

24 Y. Xie, D. W. Shaffer, A. Lewandowska-Andralojc, D. J. Szalda and J. J. Concepcion, *Angew. Chem., Int. Ed.*, 2016, **55**, 8067–8071.

25 D. W. Shaffer, Y. Xie, D. J. Szalda and J. J. Concepcion, *J. Am. Chem. Soc.*, 2017, **139**, 15347–15355.

26 R. Matheu, M. Z. Ertem, J. Benet-Buchholz, E. Coronado, V. S. Batista, X. Sala and A. Llobet, *J. Am. Chem. Soc.*, 2015, **137**, 10786–10795.

27 L. Wang, L. Duan, B. Stewart, M. Pu, J. Liu, T. Privalov and L. Sun, *J. Am. Chem. Soc.*, 2012, **134**, 18868–18880.

28 L. P. Tong, L. L. Duan, Y. H. Xu, T. Privalov and L. C. Sun, *Angew. Chem., Int. Ed.*, 2011, **50**, 445–449.

29 M. D. Karkas, T. Akermark, H. Chen, J. L. Sun and B. Akermark, *Angew. Chem., Int. Ed.*, 2013, **52**, 4189–4193.

30 Y. Pineda-Galvan, A. K. Ravari, S. Shmakov, L. Lifshits, N. Kaveevivitchai, R. Thummel and Y. Pushkar, *J. Catal.*, 2019, **375**, 1–7.

31 E. Duliere, M. Devillers and J. Marchand-Brynaert, *Organometallics*, 2003, **22**, 804–811.

32 B. Oelkers, *Eur. J. Inorg. Chem.*, 2014, 5838–5848.

33 L. Duan, L. Wang, A. K. Inge, A. Fischer, X. Zou and L. Sun, *Inorg. Chem.*, 2013, **52**, 7844–7852.

34 N. Song, J. J. Concepcion, R. A. Binstead, J. A. Rudd, A. K. Vannucci, C. J. Dares, M. K. Coggins and T. J. Meyer, *Proc. Natl. Acad. Sci. U. S. A.*, 2015, **112**, 4935–4940.

35 V. Nair and A. Deepthi, *Chem. Rev.*, 2007, **107**, 1862–1891.

36 J. Yang, J. X. An, L. P. Tong, B. H. Long, T. Fan and L. L. Duan, *Inorg. Chem.*, 2019, **58**, 3137–3144.

37 A. Gunay and K. H. Theopold, *Chem. Rev.*, 2010, **110**, 1060–1081.